Combining Anisotropic Etching and PDMS Casting for Three-Dimensional Analysis of Laser Ablation Processes

Valentine Grimaudo,*,[†] Pavel Moreno-García,[†] Alena Cedeño López,[†] Andreas Riedo,[‡]
Reto Wiesendanger,[‡] Marek Tulej,[‡] Cynthia Gruber,[§] Emanuel Lörtscher,[§] Peter Wurz,[‡]
and Peter Broekmann*,[†]

[†]Department of Chemistry and Biochemistry, University of Bern, Freiestrasse 3, CH-3012 Bern, Switzerland
[‡]Physics Institute, Space Research and Planetary Sciences, University of Bern, Sidlerstrasse 5, CH-3012 Bern, Switzerland
[§]IBM Research - Zurich, Science and Technology Department, Säumerstrasse 4, CH-8803 Rüschlikon, Switzerland

S *Supporting Information*

ABSTRACT: State-of-the-art laser ablation (LA) depth-profiling techniques (e.g. LA-ICP-MS, LIBS, and LIMS) allow for chemical composition analysis of solid materials with high spatial resolution at micro- and nanometer levels. Accurate determination of LA-volume is essential to correlate the recorded chemical information to the specific location inside the sample. In this contribution, we demonstrate two novel approaches towards a better quantitative analysis of LA craters with dimensions at micrometer level formed by femtosecond-LA processes on single-crystalline Si(100) and polycrystalline Cu model substrates. For our parametric crater evolution studies, both the number of applied laser shots and the pulse energy were systematically varied, thus yielding 2D matrices of LA craters which vary in depth, diameter, and crater volume. To access the 3D structure of LA craters formed on Si(100), we applied a combination of standard lithographic and deep reactive-ion etching (DRIE) techniques followed by a HR-SEM inspection of the previously formed crater cross sections. As DRIE is not applicable for other material classes such as metals, an alternative and more versatile preparation technique was developed and applied to the LA craters formed on the Cu substrate. After the initial LA treatment, the Cu surface was subjected to a polydimethylsiloxane (PDMS) casting process yielding a mold being a full 3D replica of the LA craters, which was then analyzed by HR-SEM. Both approaches revealed cone-like shaped craters with depths ranging between 1 and 70 μm and showed a larger ablation depth of Cu that exceed the one of Si by a factor of about 3.
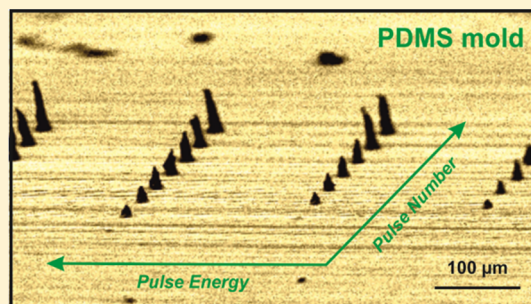
Laser ablation (LA) techniques utilizing ultrashort pulses are increasingly attracting attention in fundamental research, industry, and medicine.[1,2] The fact that any kind of solid (electrically conductive or dielectric) can be ablated within seconds without extensive and time-consuming sample preparation makes these LA-based techniques highly interesting for chemical analyses that are particularly focusing on small and locally confined sample spots (∅ at μm and sub-μm regime). These analytical techniques are applicable in various research fields ranging from the analysis of solids in geology[3,4] to the investigation of multicomponent structures in photovoltaic[5] and semiconductor industry.[6] LA inductively coupled plasma mass spectrometry (LA-ICP-MS),[5,7−10] laser ionization mass spectrometry (LIMS),[4,6,11−16] and laser-induced breakdown spectroscopy (LIBS)[9,17−19] are, among others, analytical techniques providing quantitative information on the chemical composition of solids down to trace abundances with high spatial resolution at micrometer and nanometer levels. With each laser shot, a certain volume of sample material is ablated and subsequently analyzed in the gas-phase. The successive application of laser shots on a single spot of the sample allows

for the chemical analysis of the ablated volume and its chemical reconstruction in depth. Further extending this depth profiling approach to a 2D raster mode provides means of a full chemical analysis of the sample in three dimensions.[9,10,14,17] However, the reliability of such LA-based chemical analyses crucially relies on the accurate determination of the spatial structure, e.g. the volume, of the sample material removed during LA events. This is actually the basis for a reliable correlation of chemical information (derived e.g. from the MS analysis) to specific locations inside the sample or crater and becomes particularly relevant when dealing with cavities having large (depth-to-diameter) aspect ratios. It has already been shown, however, that the spatial structure of the ablation volume can significantly deviate from an ideal cylindrical geometry.[20,21] Instead, more tapered, cone-like cross sections were observed (denoted as "craters"). Such a deviation from an ideal ablation process has considerable implications on the reconstruction of the chemical
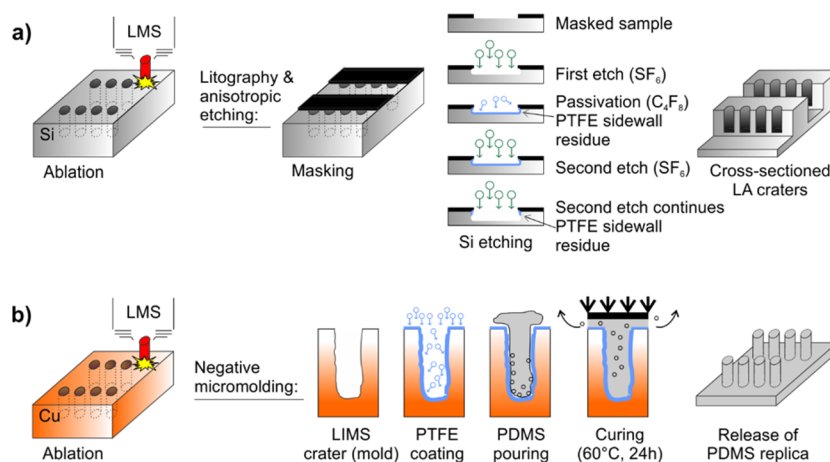
Figure 1. (a) Schematic representation of the lithographic etching approach applied to investigate the morphological characteristics of the laser-induced craters on the Si sample. Only two "Bosch" cycles are shown in the third panel of the figure. (b) Schematic representation of the PDMS-based approach applied to investigate the morphological characteristics of the laser generated craters on the Cu sample.

sample composition.[22] Additionally, element fractionation changes significantly as the crater depth evolves since condensation rate of ablated materials onto the side-walls crucially depends on the crater depth. These effects have been attributed to an ablation mechanism which changes at an advanced depth stage from photothermal- to plasma-dominated LA. Interactions between the plasma formed during the LA and the inner walls of the craters need to be taken into account in particular for aspect ratios $\geq 5-6$.[20,21] Further consequences of the irregularly shaped ablation craters are, among others, (i) a nonuniform irradiance on the illuminated surface,[20] (ii) an undesired self-focusing of the beam to the bottom of the ablated zone,[23] and (iii) the change of the ablation rate[20] as the effective illuminated area changes with progressing ablation. Understanding these effects is essential for a truly quantitative three-dimensional chemical analysis of solid materials at small spatial scales. This would further allow for parametric studies which are intended to achieve a clear correlation of specific ablation parameters (wavelength, incident angle, pulse duration, repetition rate, fluence, number of applied laser pulses, etc.)[1,24−26] to the resulting ablation volume and spatial structure of the LA craters.

To date, several methods have been employed to analyze LA craters including atomic force microscopy (AFM),[27,28] scanning electron microscopy (SEM),[29−31] white-light interferometry,[20,32−34] confocal microscopy,[35] and optical microscopy of transparent materials.[20−22] A more versatile approach is based on focused-ion beam (FIB) milling followed by SEM imaging of the cross-sectioned LA craters.[36,37] A severe drawback of this technique, however, is related to the fact that only a single crater can be subjected to the ion milling at the same time which makes the FIB approach rather time-consuming and costly in particular for more extended parametric studies on the LA crater evolution. Furthermore, ion implantation and ion channeling effects might alter the crater characteristics upon milling, thus leading to a falsified analysis of crater cross sections.

In this contribution, we report two novel strategies which allow a fast and reliable preparation of complete batches of 2D LA crater matrices (pulse energies, number of applied pulses) as basis for both a comprehensive qualitative and quantitative analysis of the LA characteristics and crater evolution.

Our first approach has its origin in industrial semiconductor processing and employs a combination of standard lithographic patterning techniques and anisotropic selective Si etching ("Bosch-process"). Applied to 2D matrices of LA craters, this approach results in well-defined rows of partially cleared LA craters that thus become accessible for cross-sectional SEM inspection.

The second approach is based on a polydimethylsiloxane (PDMS) casting process that yields a full three-dimensional mold of the previously formed crater with all its features. Instead of analyzing the original LA craters in very constraint geometries, their negative replica is analyzed by SEM. This casting technique is nondestructive, applicable to any kind of solid substrate and is employable also at intermediate LA steps. It is therefore considered much more versatile than the combined lithography and Si etching approach, which remains restricted to those (semiconductor) materials (e.g., Si) that can be etched anisotropically.

In our present study, 2D matrices of crater features were produced on Si(100) and Cu substrates by means of a femtosecond (fs) laser ablation process. The HR-SEM analysis of either the crater cross sections or the crater replica was complemented by top-down optical white-light and atomic force microscopic (AFM) inspection of the crater openings prior to the etching or casting treatments.

Both approaches discussed herein allow for a detailed quantitative description of the crater evolution process.

We expect that in particular the PDMS casting method will significantly contribute in future to a more accurate spatial analysis of trace elements in LA-based depth profiling experiments.

■ MATERIALS AND METHODS

Samples. LA craters were produced on single crystalline Si(100) and polycrystalline Cu model samples which significantly differ in their physical characteristics (e.g., thermal conductivity). The Si wafer coupons were provided by BASF Taiwan Ltd. The Cu-foil specimen was purchased from Alfa Aesar (99.9% purity, 0.254 mm thickness).

Laser Ablation. As further improvement to our previous mass spectrometric measurements using a miniature LIMS system[6,12,27] a beam shaper (focal-π shaper, AdlOptica GmbH, Germany) was introduced in the beam delivery system
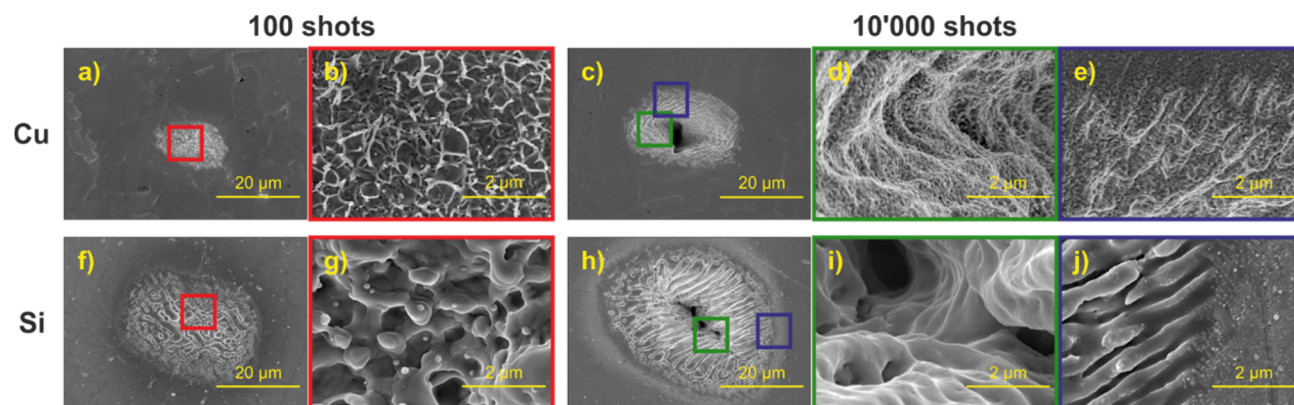
Figure 2. HR-SEM images of LA craters illustrating the distinct laser-matter interaction of Cu and Si for a pulse energy of ∼2.0 μJ and different number of applied laser shots. (a) and (f) Cu and Si crater generated with 100 consecutive laser shots each. (b) and (g) central part of Cu and Si crater, respectively, indicated by the red frame in (a) and (f). (c) and (h) Cu and Si crater formed by 10 000 laser shots each. (d) and (i) show the central part, (e) and (j) the border part of the Cu and Si crater in (c) and (h) (indicated by the green and blue frame), respectively.

converting the Gaussian profile of the laser beam from the fs-laser system ($\tau \sim 190$ fs, $\lambda = 775$ nm) into a quasi-flat-top profile at focal plane. The change in the group velocity dispersion is negligible as the material used for the optical parts in the shaper is fused silica.

The basis for our comprehensive study on the laser-matter interaction and the LA crater evolution was the systematic variation of (i) the number of applied laser shots and (ii) the laser pulse energy at multiple surface locations. For each pulse energy (varied from 0.9 to 3.3 μJ), craters were generated for a ramp of laser shots (ramped from 100 to 10 000 shots), thus leading to well-defined matrices of LA craters differing in their lateral dimension, depth, and volume.

All craters were analyzed by AFM and high-resolution-SEM (HR-SEM). Further technical details about these measurements are reported in the Supporting Information (SI).

Selective Anisotropic Etching of Silicon. To determine the morphological characteristics of fs-induced LA craters on the Si wafer, we used standard lithographic and deep reactive-ion etching techniques (DRIE). Parallel rectangular rows were lithographically patterned on the Si sample in such a way that half of the craters across their center were covered by the polymer mask (see Figure 1a, masking step, and SI Figure S5). The pitch between adjacent rectangles was identical to the pitch between craters to ensure that the subsequent etching would provide optimal matching to the craters' centers. A "Bosch-process" of alternating etching-passivation cycles was then applied to achieve ∼80 μm vertical etching of the unmasked Si surface (see third panel in Figure 1a; Alcatel 1800 W, etch rate of 5 μm/min). The resulting cross-sectioned LA craters were then analyzed by tilted SEM imaging (Hitachi S-3000N Scanning Electron Microscope (Japan), accelerating voltage of 25 keV at a working distance of 10 mm) after resist removal in acetone and cleaning in isopropanol. The results are summarized in Figure 4a, and a detailed image of a sample crater is displayed in Figure 4b (3000 shots at 1.4 μJ).

Negative Micro-Molding of Copper Craters. Because the selective anisotropic etching discussed in the previous section is suitable only for Si substrates, we employed an alternative polydimethylsiloxane (PDMS)-based approach to obtain a three-dimensional replica of the LA craters on the Cu sample (see Figure 1b). This approach allows the fabrication of flexible structures in the micrometer and sub-micrometer range

for microcontact printing and three-dimensional replica molding.[38]

In a first step, a thin (octafluorocyclobutane-based) antiadhesion coating (∼50 nm) was deposited on the Cu sample to avoid undesirable sticking between the PDMS and the Cu substrate after baking. A custom-made mixture of polydimethylsiloxane (PDMS) derivative (Sylgard 184 from Sigma-Aldrich), was then poured over the Cu surface inside a Teflon-coated Aluminum compartment, filling the ablated cavities. To cure the resin, the stack was placed inside a vacuum furnace where the temperature was set to 60 °C for a duration of 12 h. This way any enclosed gas inside the PDMS material or captured below the PDMS in enclosed volumes, e.g. at the craters' bottom, is released by diffusion through the PDMS and a conformal replica is casted. Finally, the negative PDMS mold was gently released from the Cu sample providing a nanometer-accurate template of the ablated cavities of the Cu substrate. This way, even the back-bending at the bottom of the craters was reproduced. The high elasticity of PDMS mold avoids inelastic deformation of the Cu replica during the stripping.[38] To study the characteristic dimensions of the PDMS negative by tilted SEM imaging, the mold was coated by a thin 5 nm Au/Pd conductive metal layer preventing any charge accumulations on the surface by the released electrons (see panels c and d in Figure 4, Zeiss Leo SEM, 3 kV acceleration voltage, 30 μm aperture).

■ RESULTS AND DISCUSSION

Top-Down Crater Analysis. The LA characteristics for Si and Cu target materials were comprehensively investigated by means of top-down SEM inspection and complementary AFM analysis. Figure S-1 shows optical microscope images with a survey of crater arrays on the Cu and the Si sample, respectively, generated by a systematic variation of the laser pulse energy (0.9−3.3 μJ) and the total number of laser pulses (100−10 000). Figure 2 displays representative top-down SEM images of Cu (panels a and c) and Si (panels f and h) samples after applying 100 and 10 000 laser shots at pulse energies of ∼2.0 μJ. From the SEM inspection, it becomes obvious that the total surface area affected by the laser beam is much more extended for Si than for Cu. However, the deeper central parts of these zones have in both cases similar lateral dimensions. We consider those areas affected by the laser beam as "craters" where massive ablation of substrate material takes place upon
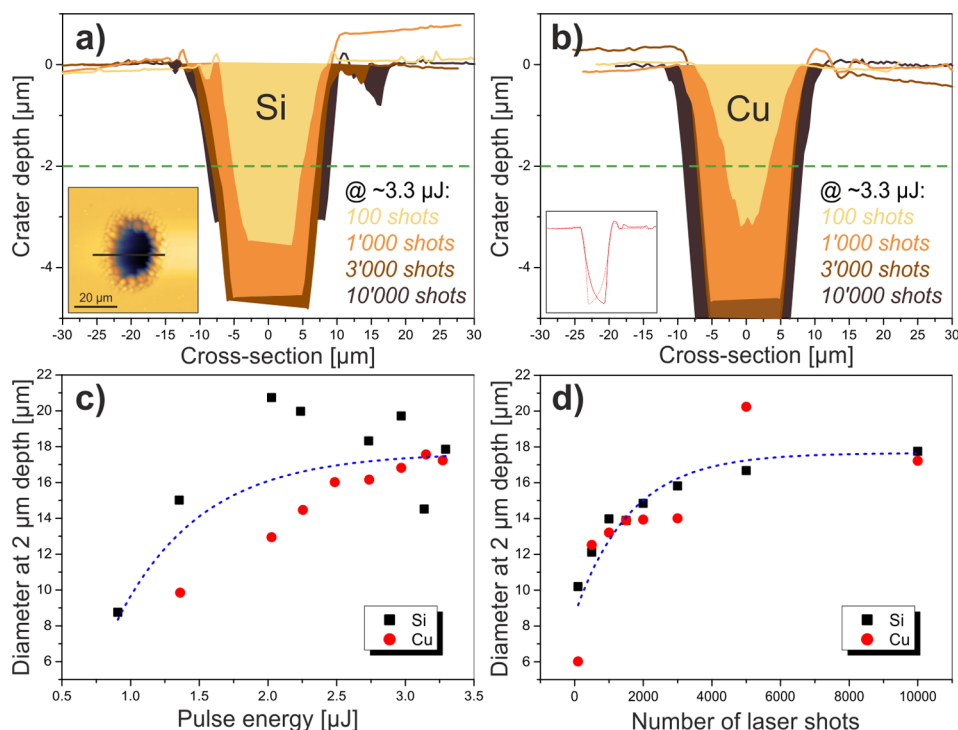
Figure 3. Panels (a) and (b) show cross-sectional AFM depth profiles of Si and Cu craters recorded along the scanning line indicated in the inset image of panel a). Panels (c) and (d) show the crater diameter measured at 2 μm crater depth (green dotted line in panels a and b) as a function of pulse energy for 10 000 laser shots and as a function of applied laser shots for a pulse energy of ~3.3 μJ, respectively. The blue dotted line only serves to guide the eye and should illustrate a nonlinear behavior of the data evolution.

laser irradiation, whereas significant changes in the surface morphology might occur in the outer parts of the zones affected by the laser light even without any net removal of sample material. Irradiation of the Cu and the Si surfaces by the fs-laser beam leads in both cases to crater features having an elliptical appearance (Figure 2c,h). We attribute the observed elliptical crater shape to the particular polarization characteristics of the used laser light (linear)[39] and to the current optical beam guiding system.

The application of only 100 laser pulses resulted on both materials in rather shallow depressions. In this initial stage of the LA process the Cu crater consists of a dense network of elongated and curved ripples which are randomly distributed (see panel b of Figure 2). These morphological features show pronounced similarities to nanoprotrusions and nanocavities reported by Vorobyev et al. for Pt and other metallic surfaces.[40] In contrast to Cu, we observe on Si larger droplet-like features in the initial stage of crater formation (Figure 2g).

Differences in the lateral dimensions of zones affected by the laser pulses are more apparent in the initial stage of crater development (100 laser shots) than in a more advanced stage of the LA process (10 000 laser shots). These differences in the dimensions of the affected zones can be rationalized on the basis of the material specific thermal conductivity which is substantially higher in case of Cu (see Table-S1).[41] A higher thermal conductivity implies much faster and more effective dissipation of heat into the bulk material, therefore resulting in a spatially and temporally more confined impact of repetitive laser pulses on the sample surface.

In particular, the wings of the quasi-flat-top laser pulse whose energy is below the actual ablation threshold can induce severe morphological changes in the peripheral zones affected by the laser pulse even without any net removal of sample material.

These heat-mediated morphological damages are more pronounced and laterally more extended for materials like Si having a lower thermal conductivity. These morphological changes often go along with significant changes in the local optical properties of the material. An increased surface roughness typically leads to a more effective absorption of laser light, which further reduces the so-called "damage threshold".

This kind of incubation phenomena was already reported in the literature.[42] They were found to alter the optical properties of the material even for laser pulses as short as 5 fs.[42] Typically the time scale of the exciting laser pulse in these experiments is about 3 orders of magnitude shorter than the one on which vibrational excitations (lattice heating) take place. This is the reason why the heat affected zone (HAZ) is significantly reduced when using sub-ps pulses. However, the initial electron heating leads to an electron–phonon coupling which can thermally alter the close vicinity (few nm) of the generated LA crater.[43]

Figure 2d–e, i–j display HR-SEM images of those sections of the LA crater features (10 000 laser shots) highlighted by green and blue frames in panels c and h. The LA crater formed in the Si substrate exhibits a nm-smooth surface appearance. In addition, so-called laser-induced periodic surface structures (LIPSSs), such as ripples and columns, are visible on the μm length scale.[44] This surface pattern might originate from the interference of the incident laser beam with a surface electromagnetic wave (SEMW) of the target material that involves the collective excitation of electron modes (e.g., surface plasmon polaritons (SPPs)).[45,46] A further difference in the crater characteristics of Si and Cu concerns a bright rim surrounding the LA craters on the Si sample. At higher magnification in the SEM inspection (Figure 2j), one can
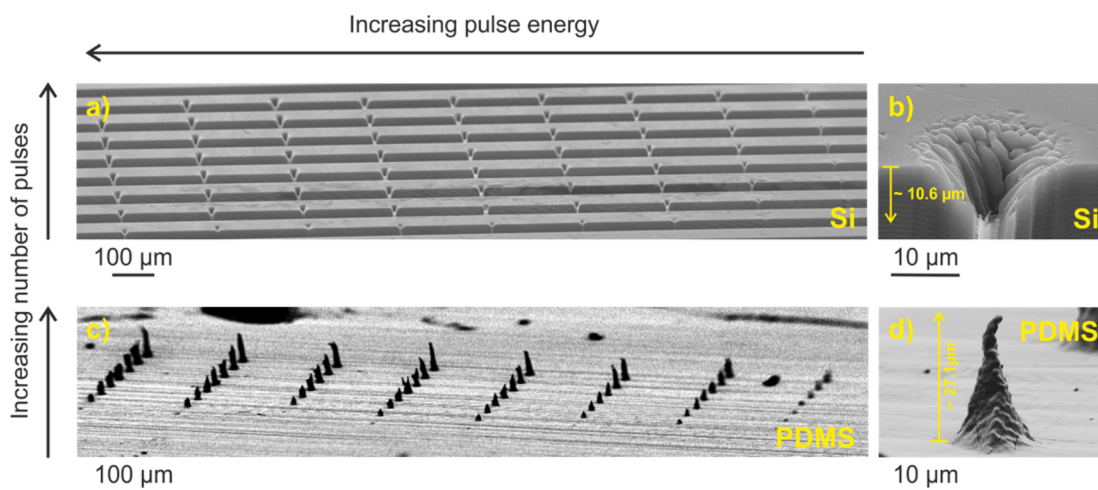
Figure 4. (a) and (c) SEM overview of Si crater cross sections obtained by the "Bosch-process" and PDMS mold of the Cu craters. Magnified SEM images showing a typical (b) cross-section of a Si crater and (d) PDMS mold of a Cu crater (3000 shots at ~1.4 μJ). Both approaches enabled the determination of the crater depth and profile for different applied measurement conditions (pulse energies and number of laser shots).

ascribe these structural features to resputtered Si nanoparticles (~100 nm in size). Such resputtering effects were not observed for the Cu sample. In contrast to the Si, the Cu craters exhibit a rougher surface appearance on the nm scale. A certain kind of extended, μm-sized LIPSS features are also present at the opening and the side-walls of the Cu crater (Figure 2d), but to a lesser extent than observed for Si. They are most likely formed by the growth and subsequent coalescence of so-called nanotubes (Figure 2b) by increasing the number of applied laser pulses.[40] An overview of all top-down SEM images of the Si and Cu craters is provided in the SI file (see Figures S-2–S-3)

Further structural characterization of the crater openings was conducted by means of AFM (Figure 3). Note that due to the large aspect ratio of the LA craters the AFM methodology is reliable only for crater depths down to ~4 μm. All LA craters were analyzed along the two main symmetry axes of the elliptical cavities (ratio of both axes is about 0.8). For the sake of simplicity we show here only those AFM measurements recorded along the scanning direction hitting the center of the craters as indicated in the inset figure of Figure 3a. Panels a and b in Figure 3 present topographic profiles of LA craters generated after applying 100, 1000, 3000, and 10 000 laser shots at a pulse energy of 3.3 μJ. Note that the smaller depth for the crater formed by 10 000 laser shots shown in Figure 3a emerges due to AFM measurement artifacts and is in fact deeper than the other presented craters. To avoid artifacts in the AFM imaging related to the large aspect ratio, the presented crater profiles result from the superposition of forward and backward AFM scans as illustrated by the inset in Figure 3b. The AFM results indicate LA crater profiles in close vicinity of the crater opening, which are only weakly affected by the total number of applied laser shots (n). This observation supports the quasi-flat-top nature of the employed fs-laser beam. The observed secondary depressions around the major crater are below one micrometer in depth, and are believed to be an accumulation of LIPSS features, which may emerge from the beam wings.

Figure 3c presents the dependence of the LA crater diameters at a depth of 2 μm on the laser pulse energies. For Cu there is clearly a nonlinear increase of the crater diameter in the range of lower pulse energies, which, however, reaches a plateau regime at larger pulse energies. Because the crater diameter is determined by the shape of the laser pulse profile, the origin of the plateau is most likely due to the steep walls of our quasi-flat-top pulse profile, whereas the initial steep increase of the curve is indicative for a slight deviation from the ideal flat-top shape of the laser beam dominating the crater evolution characteristics particularity at lower pulse energies. Note that the scatter of the respective AFM data for Si does not allow any conclusive statement for the Si craters.

The plot in panel d of Figure 3 illustrates the dependence of the crater diameter on the total number of applied laser shots at constant applied pulse energy of 3.3 μJ. Contrary to what is expected from a Gaussian beam profile,[28] only a moderate change of the crater diameters with the applied number of laser shots is observed for Si and Cu craters. An increase of the crater diameter for both materials is solely noticeable in the initial phase of the crater evolution process before entering a plateau regime at higher numbers of laser shots. These findings are indicative for LA mechanism which might change as the crater evolves.

Both target materials form craters with similar diameters upon increasing pulse energies and increasing number of applied laser shots, at least within the investigated ranges.

Advanced Crater Analysis. To go beyond a pure top-down crater inspection we applied two advanced preparation methods to unravel the depth and the full three-dimensional shape of the formed LA craters. The first one was based on a lithographic approach followed by a selective and anisotropic, wet chemical etching process of Si leaving behind cross-sectioned LA craters. The second one applied to the Cu sample was based on a PDMS process yielding a full three-dimensional replica as casting mold of the crater features (for details see section Materials and Methods).

Survey SEM images of the analyzed matrices of crater cross sections and molds are presented in Figure 4a,c. Representative SEM images of a closed-up single cross-sectioned Si crater and a single Cu crater replica are shown in Figure 4b,d, respectively. Both craters were produced by applying the same number of 3000 laser shots at constant pulse energy of 1.4 μJ. Our SEM analysis reveals for both cases a distinct conical shape of the LA craters, although the laser beam has been optimized for a quasi-flat-top beam profile prior to the LA treatment. LIPSS features
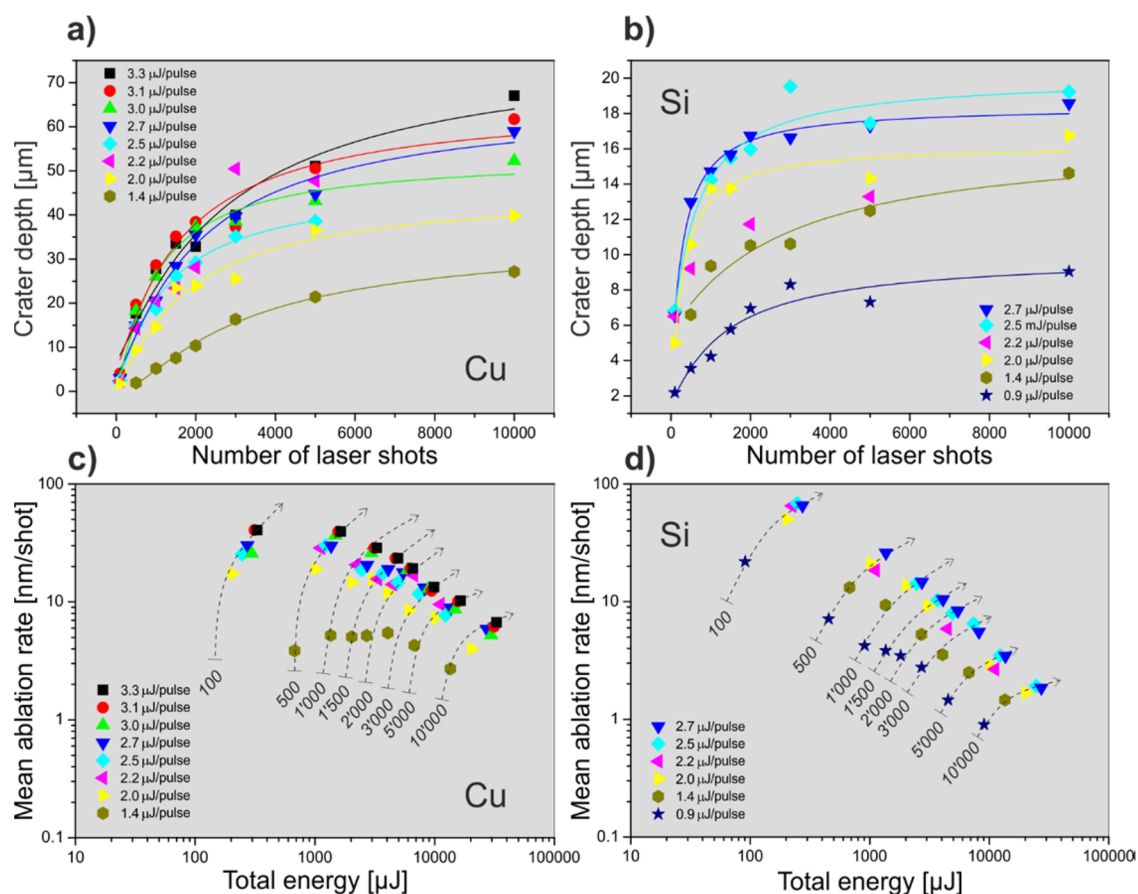
Figure 5. Panels (a) and (b) show ablation depths as a function of the applied laser shots for different applied pulse energies. Panels (c) and (d) present the changes of the mean ablation rate, calculated over the crater depth, for different pulse energies, with increasing applied total energy (number of laser shots times the pulse energy).

already observed in the top-down SEM crater inspection (Figure 2) are also clearly visible at the interior side-walls of the crater features (Figure 4b) and on the outer surface of the PDMS mold (Figure 4d), the latter representing the morphology of the side-walls inside the respective Cu crater.[1]

A comprehensive analysis of the obtained SEM data was used as basis for a detailed quantification of the LA characteristics on Si and Cu. Results are presented in Figure 5 for a number of total laser shots ranging from 100 to 10 000 and pulse energies that were varied from 0.9 to 3.3 μJ. Note that due to a slight misalignment of the polymer mask during the Si etching process, craters formed at pulse energies of 3.0−3.3 μJ were not cross-sectioned properly during the process and were therefore not included into our analysis. Data presented in panels a and b of Figure 5 indicate LA depths, which are 3 times lower for Si as compared with Cu.

Electrons are excited in the semiconducting Si from the occupied valence band to the unoccupied conduction band with a photon energy that exceeds the bandgap, whereas in metals the light absorption primarily proceeds via free electrons from the conduction band. Therefore, higher energy densities are required for Si to generate free electrons.[47]

From a thermodynamic point of view one can assume in a first approximation a scaling of the ablation and ionization for a specific material with (i) its melting/boiling point, (ii) its atomization enthalpy, and (iii) its (first, second) ionization energy. The atomization enthalpy is the minumum energy needed to break chemical bonds in the solid and to promote

the constituting atoms/molecule from the solid to the gaseous phase. From this simplified considerations (see Table S-1) one would indeed expect a higher ablation rate for Cu than for Si.

For both materials, the crater depth scales with the applied pulse energy and shows an inverse exponential dependence on the applied number of laser shots. This behavior is fully consistent with a LA rate that decreases as a function of the crater depth and with the evolution of conical crater geometries. For the very initial phase of crater evolution (first few laser shots), there is a distinct correlation between the LA rate and the total applied energy (Figure 5c,d). For Cu, we observe a constant LA rate for up to 500 laser shots. Interestingly, for the first 100 laser pulses the LA rate of Si is by a factor of about 2 higher as compared to the one of Cu. The LA rate of Si drops down much faster upon increasing number of applied laser shots than the one of Cu, resulting in lower crater depths in the Si for an advanced stage of the crater evolution. Further information about the dependence of the total area affected by the laser irradiation (determined by top-down SEM analysis) on the total applied energy can be found in the SI (see Figure S-4).

A preliminary determination of the crater volumes (Figure 6) was based on the obtained SEM and AFM data (crater depths and crater diameters) under the simplifying assumption of an ideally conical shape of the formed LA craters. A possible explanation for the resulting conical shape of the craters could be related to the nature of the applied telescope that is used for the transformation of the initial Gaussian beam to the flat-top
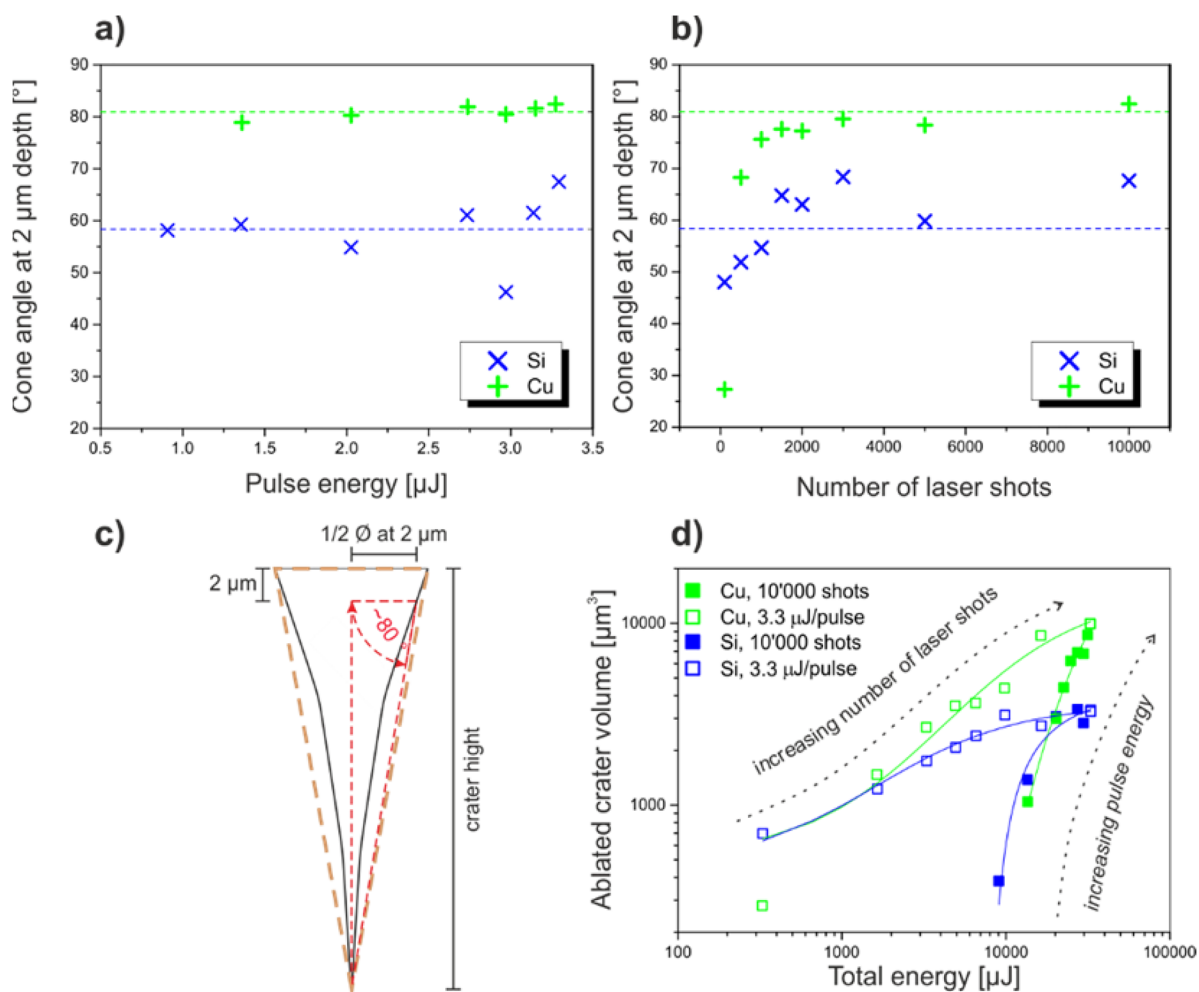
Figure 6. Panels (a) and (b) present the calculated cone angle from the red dotted line in (c) derived from the measured radius and depth at 2 μm crater depth as a function of the applied pulse energy or number of shots, respectively. Panel (c): Sketch of the cross-section of the crater illustrating the difference between the real shape, indicated by the solid black line, and the simplified modeled cone shape shown as brown dotted line. The red dotted line shows the crater radius at 2 μm depth measured by AFM. Panel (d): Ablated crater volumes for Si and Cu craters assuming an elliptical cone shape represented in (c) by the brown dotted triangle.

profile. The beam after the beam shaper undergoes a sequence of interferometric patterns, which should create in the lens' focal plane a profile that is close to a flat-top profile. Displacement from the focal plane modifies the pulse profile up to the restoration of a Gaussian-like beam profile. This would require a constant adjustment of the focusing lens, which at this state is not applicable due to the instrument design.

A more precise profile determination can be done by extracting the PDMS profile from SEM images, as exemplarily performed for one prototypical crater mold presented in the SI (see Figure S-6). However, such high-accurate image extractions and direct experimental determination of the crater volumes (e.g., by means of confocal microscopy, white-light interferometry, or micro-CT) is beyond the scope of our present paper and will therefore be addressed separately in a forthcoming communication.

Panels a and b in Figure 6 show the calculated wall angle (i) as a function of applied pulse energy for a constant number of laser shots and (ii) as a function of the number of applied laser shots at a constant pulse energy. The calculated cone angles at 2 μm crater depth (see red dotted line in Figure 6c for the illustration of the angle) are clearly larger for Cu than for Si. Moreover, upon applying a constant large number of laser shots

for different pulse energies the angle of the assumed cone crater seems to fluctuate much less for Cu than for Si (Figure 6a). However, for low numbers of laser shots, the cone angle depends exponentially on the amount of deposited energy and therefore on the initial crater formation step (Figure 6b). This implies that the ratio between the base and the depth of the craters is almost constant for different applied pulse energies once the crater shape has been established.

Figure 6d shows the increase of the crater volume with increasing energy dose. It becomes obvious that, at a given energy dose, the LA craters on Cu are much bigger in volume than the ones formed on the Si substrate thus pointing to LA processes which are much more effective on Cu than on Si (as expected from the specific material characteristics). The open squares in Figure 6d represent the evolution of the crater volumes with increasing number of laser shots for constant pulse energies of ~3.3 μJ, whereas the filled symbols depict crater volumes as a function of the pulse energy at a constant number of applied laser shots (10 000). In both types of experiments, the resulting dependence of the ablated volume decreases with increasing total energy dose.

CONCLUSIONS

Anisotropic Si etching and PDMS casting techniques enable a fast and reliable processing of two-dimensional arrays of LA craters (about 80 craters per sample in this study) with the aim of a systematic both qualitative and quantitative analysis of the crater evolution. These new preparation techniques allow for a direct correlation of the applied laser conditions (number of laser shots and pulse energy) and the resulting crater morphologies.

Regardless of the sample material (Si or Cu) and the particular preparation technique applied, our results clearly demonstrate the formation of cone-shaped crater geometries upon laser−matter interaction. Characteristic LIPSS features imaged on the crater openings by conventional top-down SEM inspection could now be observed even in the interior of the LA craters. Our novel LA crater preparation schemes provide a broad experimental platform for a deeper understanding of laser-matter interaction in general and allow for the determination of various quantities that are important for the LA process such as the mean ablation rate and the crater volumes. Important to note is that in particular the PDMS casting approach is nondestructive and therefore allows a repetitive formation of crater replica. Furthermore, this technique is much more versatile and applicable to a variety of materials, whereas the etching process remains restricted to those sample materials which can be selectively and anisotropically etched by wet chemical processing (e.g., Si). Another drawback of the DRIE technique is that the obtained cross-sectional information is restricted to one axis of the crater only and that this information relies on the precise etching along the center of the crater. For slightly asymmetric craters this etching procedure may result in incomplete depth profiles.

The novel preparation techniques were applied to Si and Cu model substrates. As expected from the material characteristics, our quantitative crater volume and crater depth analysis revealed LA rates that are larger for Cu than for Si.

Future work will particularly focus on the more accurate determination of the LA crater volumes on the basis of PDMS replica by using advanced three-dimensional optical microscopy and micro X-ray computer tomography.

ASSOCIATED CONTENT

Ⓢ Supporting Information
The Supporting Information is available free of charge on the ACS Publications website at DOI: 10.1021/acs.anal-chem.7b04539.

> Surveys of optical microscope and top-down SEM images of all Si and Cu craters, technical details of crater imaging measurements, an optical microscope image of the lithographical mask, correlation plots of laser affected area and total applied energy, microscale side-wall angle determination, and a table with various Si and Cu material properties (PDF)

AUTHOR INFORMATION

Corresponding Authors
*E-mail: valentine.grimaudo@dcb.unibe.ch. Phone: +41 31 631 43 17.
*E-mail: peter.broekmann@dcb.unibe.ch.

ORCID Ⓞ
Valentine Grimaudo: 0000-0002-7010-5903
Andreas Riedo: 0000-0001-9007-5791
Peter Broekmann: 0000-0002-6287-1042

Notes
The authors declare no competing financial interest.

ACKNOWLEDGMENTS

REFERENCES

(1) Bonse, J.; Baudach, S.; Krüger, J.; Kautek, W.; Lenzner, M. *Appl. Phys. A: Mater. Sci. Process.* **2002**, *74*, 19−25.

(2) Guizard, S.; Semerok, A.; Gaudin, J.; Hashida, M.; Martin, P.; Quéré, F. *Appl. Surf. Sci.* **2002**, *186*, 364−368.

(3) Huang, R.; Zhang, B.; Zou, D.; Hang, W.; He, J.; Huang, B. *Anal. Chem.* **2011**, *83*, 1102−1107.

(4) Tulej, M.; Neubeck, A.; Ivarsson, M.; Riedo, A.; Neuland, M. B.; Meyer, S.; Wurz, P. *Astrobiology* **2015**, *15*, 669−682.

(5) Gutiérrez-González, A.; González-Gago, C.; Pisonero, J.; Tibbetts, N.; Menéndez, A.; Vélez, M.; Bordel, N. *J. Anal. At. Spectrom.* **2015**, *30*, 191−197.

(6) Riedo, A.; Grimaudo, V.; Moreno-Garcia, P.; Neuland, M. B.; Tulej, M.; Wurz, P.; Broekmann, P. *J. Anal. At. Spectrom.* **2015**, *30*, 2371−2374.

(7) Van Malderen, S. J. M.; van Elteren, J. T.; Vanhaecke, F. *Anal. Chem.* **2015**, *87*, 6125−6132.

(8) Wang, H. A. O.; Grolimund, D.; Giesen, C.; Borca, C. N.; Shaw-Stewart, J. R. H.; Bodenmiller, B.; Günther, D. *Anal. Chem.* **2013**, *85*, 10107−10116.

(9) Chirinos, J. R.; Oropeza, D. D.; Gonzalez, J. J.; Hou, H.; Morey, M.; Zorba, V.; Russo, R. E. *J. Anal. At. Spectrom.* **2014**, *29*, 1292−1298.

(10) van Elteren, J. T.; Izmer, A.; Sala, M.; Orsega, E. F.; Selih, V. S.; Panighello, S.; Vanhaecke, F. *J. Anal. At. Spectrom.* **2013**, *28*, 994−1004.

(11) Kuznetsov, I.; Filevich, J.; Dong, F.; Woolston, M.; Chao, W.; Anderson, E. H.; Bernstein, E. R.; Crick, D. C.; Rocca, J. J.; Menoni, C. S. *Nat. Commun.* **2015**, *6*, 6944.

(12) He, M.; Meng, Y.; Yan, S.; Hang, W.; Zhou, W.; Huang, B. *Anal. Chem.* **2017**, *89*, 565−570.

(13) Grimaudo, V.; Moreno-García, P.; Riedo, A.; Neuland, M. B.; Tulej, M.; Broekmann, P.; Wurz, P. *Anal. Chem.* **2015**, *87*, 2037−2041.

(14) Grimaudo, V.; Moreno-García, P.; Riedo, A.; Meyer, S.; Tulej, M.; Neuland, M. B.; Mohos, M.; Gütz, C.; Waldvogel, S. R.; Wurz, P.; Broekmann, P. *Anal. Chem.* **2017**, *89*, 1632−1641.

(15) Green, T.; Kuznetsov, I.; Willingham, D.; Naes, B. E.; Eiden, G. C.; Zhu, Z.; Chao, W.; Rocca, J. J.; Menoni, C. S.; Duffin, A. M. *J. Anal. At. Spectrom.* **2017**, *32*, 1092−1100.

(16) Cui, Y.; Moore, J. F.; Milasinovic, S.; Liu, Y.; Gordon, R. J.; Hanley, L. *Rev. Sci. Instrum.* **2012**, *83*, 093702.

(17) Hou, H.; Cheng, L.; Richardson, T.; Chen, G.; Doeff, M.; Zheng, R.; Russo, R.; Zorba, V. *J. Anal. At. Spectrom.* **2015**, *30*, 2295−2302.

(18) Zorba, V.; Mao, X.; Russo, R. E. *Spectrochim. Acta, Part B* **2011**, *66*, 189−192.

(19) Zorba, V.; Mao, X.; Russo, R. E. *Spectrochim. Acta, Part B* **2015**, *113*, 37−42.

(20) Borisov, O. V.; Mao, X.; Russo, R. E. *Spectrochim. Acta, Part B* **2000**, *55*, 1693−1704.

(21) Eggins, S. M.; Kinsley, L. P. J.; Shelley, J. M. G. *Appl. Surf. Sci.* **1998**, *127*, 278−286.

(22) Mank, A. J. G.; Mason, P. R. D. *J. Anal. At. Spectrom.* **1999**, *14*, 1143−1153.

(23) Lowndes, D. H.; Fowlkes, J. D.; Pedraza, A. J. *Appl. Surf. Sci.* **2000**, *154*, 647−658.

(24) Guosheng, Z.; Fauchet, P. M.; Siegman, A. E. *Phys. Rev. B: Condens. Matter Mater. Phys.* **1982**, *26*, 5366−5381.

(25) Young, J. F.; Sipe, J. E.; van Driel, H. M. *Phys. Rev. B: Condens. Matter Mater. Phys.* **1984**, *30*, 2001−2015.

(26) Seifert, G.; Kaempfe, M.; Syrowatka, F.; Harnagea, C.; Hesse, D.; Graener, H. *Appl. Phys. A: Mater. Sci. Process.* **2005**, *81*, 799−803.

(27) Hwang, D. J.; Jeon, H.; Grigoropoulos, C. P.; Yoo, J.; Russo, R. E. *Appl. Phys. Lett.* **2007**, *91*, 251118.

(28) Riedo, A.; Neuland, M.; Meyer, S.; Tulej, M.; Wurz, P. *J. Anal. At. Spectrom.* **2013**, *28*, 1256−1269.

(29) Yu, Q.; Cao, Z.; Li, L.; Yan, B.; Hang, W.; He, J.; Huang, B. *Anal. Chem.* **2009**, *81*, 8623−8626.

(30) Huang, R.; Yu, Q.; Li, L.; Lin, Y.; Hang, W.; He, J.; Huang, B. *Mass Spectrom. Rev.* **2011**, *30*, 1256−1268.

(31) Raillard, B.; Gouton, L.; Ramos-Moore, E.; Grandthyll, S.; Müller, F.; Mücklich, F. *Surf. Coat. Technol.* **2012**, *207*, 102−109.

(32) Russo, R. E.; Mao, X.; Liu, H.; Gonzalez, J.; Mao, S. S. *Talanta* **2002**, *57*, 425−451.

(33) Russo, R. E.; Mao, X.; Gonzalez, J. J.; Mao, S. S. *J. Anal. At. Spectrom.* **2002**, *17*, 1072−1075.

(34) Gonzalez, J. J.; Fernandez, A.; Oropeza, D.; Mao, X.; Russo, R. E. *Spectrochim. Acta, Part B* **2008**, *63*, 277−286.

(35) Choi, J.-H.; Moon, Y.; Lee, S.-H.; In, J.-H.; Jeong, S. *International Journal of Precision Engineering and Manufacturing-Green Technology* **2016**, *3*, 167−171.

(36) D'Abzac, F.-X.; Seydoux-Guillaume, A.-M.; Chmeleff, J.; Datas, L.; Poitrasson, F. *J. Anal. At. Spectrom.* **2012**, *27*, 99−107.

(37) Quintana, I.; Dobrev, T.; Aranzabe, A.; Lalev, G.; Dimov, S. *Appl. Surf. Sci.* **2009**, *255*, 6641−6646.

(38) Menard, E.; Rogers, J. In *Springer Handbook of Nanotechnology*; Bhushan, B., Ed.; Springer: Berlin, 2007; pp 279−298.

(39) Nolte, S.; Momma, C.; Kamlage, G.; Ostendorf, A.; Fallnich, C.; von Alvensleben, F.; Welling, H. *Appl. Phys. A: Mater. Sci. Process.* **1999**, *68*, 563−567.

(40) Vorobyev, A. Y.; Makin, V. S.; Guo, C. *J. Appl. Phys.* **2007**, *101*, 034903.

(41) Lide, D. R. *CRC Handbook of Chemistry and Physics* 84th ed.; CRC Press: New York, 2003−2004.

(42) Lenzner, M.; Krausz, F.; Krüger, J.; Kautek, W. *Appl. Surf. Sci.* **2000**, *154*, 11−16.

(43) Rethfeld, B.; Ivanov, D. S.; Garcia, M. E.; Anisimov, S. I. *J. Phys. D: Appl. Phys.* **2017**, *50*, 193001.

(44) Costache, F.; Kouteva-Arguirova, S.; Reif, J. *Appl. Phys. A: Mater. Sci. Process.* **2004**, *79*, 1429−1432.

(45) Bonse, J.; Rosenfeld, A.; Krüger, J. *J. Appl. Phys.* **2009**, *106*, 104910.

(46) Abere, M. J.; Zhong, M.; Krüger, J.; Bonse, J. *MRS Bull.* **2016**, *41*, 969−974.

(47) Rethfeld, B.; Sokolowski-Tinten, K.; von der Linde, D.; Anisimov, S. I. *Appl. Phys. A: Mater. Sci. Process.* **2004**, *79*, 767−769.